

Ultra-Strong Gradient Diffusion MRI with Self-Supervised Learning for Prostate Cancer Characterization

Tanishq Patil¹, Snigdha Sen², Malwina Molendowska^{3,4}, Kieran G. Foley⁵, Fabrizio Fasano^{6,7}, Mara Cercignani³, Marco Palombo^{3,8}, Paddy J. Sator^{3,8}, and Eleftheria Panagiotaki²

1. Department of Computer Science, University College London (UCL), London, United Kingdom
2. UCL Hawkes Institute, Department of Computer Science, University College London (UCL), London, United Kingdom
3. Cardiff University Brain Research Imaging Centre (CUBRIC), School of Psychology, Cardiff University, Cardiff, United Kingdom
4. Medical Radiation Physics, Clinical Sciences Lund, Lund University, Lund, Sweden
5. Division of Cancer and Genetics, School of Medicine, Cardiff University, Cardiff, United Kingdom
6. Siemens Healthcare Ltd, Camberly, United Kingdom
7. Siemens Healthcare GmbH, Erlangen, Germany
8. School of Computer Science and Informatics, Cardiff University, Cardiff, United Kingdom

Correspondence: Tanishq Patil; tanishq.patil.24@ucl.ac.uk
Snigdha Sen; snigdha.sen.20@ucl.ac.uk

Word Count: 4821

1 Abstract

Diffusion MRI (dMRI) enables non-invasive assessment of prostate microstructure but conventional dMRI metrics such as the Apparent Diffusion Coefficient in multiparametric MRI (mpMRI) lack specificity to underlying histology. Integrating dMRI with the compartment-based biophysical VERDICT (Vascular, Extracellular, and Restricted Diffusion for Cytometry in Tumours) framework offers richer microstructural insights, though clinical gradient systems (40–80 mT/m) often suffer from poor signal-to-noise ratio (SNR) at stronger diffusion weightings due to prolonged echo times. Ultra-strong gradients (up to 300 mT/m) can mitigate these limitations by improving SNR and contrast-to-noise ratios (CNR) but their adoption has until recently been limited to research environments due to challenges with peripheral nerve stimulation thresholds and gradient non-uniformity. This study investigates whether physics-informed self-supervised VERDICT (ssVERDICT) fitting applied to ultra-strong gradients enhances prostate microstructural characterization relative to current clinical acquisitions. We developed enhanced ssVERDICT fitting approaches using dense multilayer perceptron (Dense MLP) and convolutional U-Net architectures, benchmarking them against non-linear least-squares (NLLS) VERDICT fitting, original ssVERDICT implementation, and Diffusion Kurtosis Imaging across clinical- to ultra-strong gradient systems. Dense ssVERDICT at ultra-strong gradient notably outperformed NLLS VERDICT, boosting median CNR by 47%, cutting inter-patient Coefficient of Variation by 52%, and reducing pooled f_{ic} variation by 50%. Overall, it delivered the highest CNR, the most stable parameter estimates, and the clearest tumour-normal contrast compared with

conventional methods and clinical gradient systems. These findings highlight the potential of advanced gradient systems and deep learning-based modelling to improve non-invasive prostate cancer characterization and reduce unnecessary biopsies. With the recent adoptions of ultra-strong gradient MRI in clinical systems, these advances in prostate imaging are now well positioned for translation from research to clinical practice.

2 Introduction

Prostate cancer is the second most commonly diagnosed cancer in men worldwide [1], traditionally assessed through histological examination of excised prostate tissue. Although accurate, biopsies are invasive and carry risks for patients [2]. Diffusion MRI offers a non-invasive alternative by probing the diffusion of water molecules to reveal tissue microstructure [3]. Historically, diffusion MRI in the prostate has relied on mathematical models such as Apparent Diffusion Coefficient (ADC) and Diffusion Kurtosis Imaging (DKI) [4, 5]. While effective for capturing Gaussian and non-Gaussian diffusion respectively, these approaches do not directly relate the MR signal to underlying tumour microstructure.

Biophysical models extend these capabilities by modelling tissue as a set of distinct cellular compartments aiming to link their diffusion properties to key microstructural features like cell density, size, and spatial organization [6]. The Vascular, Extracellular, and Restricted Diffusion for Cytometry in Tumours (VERDICT) model [2] is an advanced biophysical framework that models distinct tissue compartments and can estimate their volume fractions, diffusivities, and cell radius. This framework has shown to produce parameter estimates that are in strong agreement with the ex vivo histological analysis for prostate tissue [7, 8].

Traditionally, parameter estimation for biophysical diffusion models has relied on solving complex inverse problems [9] using non-linear least squares (NLLS) fitting, which is computationally expensive and prone to instability and local minima [10-12]. More recently, supervised deep learning has emerged as a faster and more flexible alternative, although its performance remains constrained by the statistical properties of the training data distribution, leading to biased estimates on unseen test data [13, 14]. Self-supervised learning addresses this limitation by learning directly from the input signal without requiring explicit labels, improving robustness and generalizability [11, 15]. Building on this paradigm, self-supervised VERDICT (ssVERDICT) integrates physics-based [16-18] self-supervised forwards models with the VERDICT framework and has demonstrated improved tumour conspicuity and discrimination between normal and cancerous prostate tissue in prior work [11].

Sen et al. (2024) [11] demonstrated the use of ssVERDICT for prostate cancer characterization using clinical gradient strength diffusion MRI; however, such acquisition systems are restricted in the gradient strength-diffusion time ($G\Delta$) coverage, and may yield suboptimal image quality and parameter estimation. Recently, Molendowska et al. [19] addressed these limitations by adapting ultra-strong gradients (up to 300 mT/m), which had previously been restricted to head only systems, for prostate imaging. This enabled dMRI acquisition at higher b-values with significantly shorter echo times (TE), and improved signal-to-noise ratio (SNR) and contrast-to-noise ratio (CNR), particularly for early-stage prostate cancer. Their study established that high-gradient diffusion MRI is both technically viable and clinically beneficial for prostate cancer, enhancing overall diagnostic accuracy.

This study aims to apply physics-informed self-supervised VERDICT fitting to ultra-strong gradient dMRI, leveraging the complementary benefits of advanced acquisition and biophysical modelling to enhance non-invasive microstructural characterization of prostate cancer. Ultra-strong gradient

acquisition systems have been so far confined to research settings and not yet available in clinical practices due to limiting factors arising from lower peripheral nerve stimulation (PNS) threshold in subjects, gradient non-uniformity in achieving high gradient amplitudes, and image distortions from concomitant fields and eddy currents [19, 20]. With the recent availability of commercial clinical systems capable of generating gradients up to 200 mT/m, it is now an opportune moment to investigate whether the VERDICT framework can leverage ultra-strong gradients to enhance sensitivity, enabling more precise characterization of prostate microstructure and improved differentiation between malignant and normal tissues compared to conventional clinical gradient acquisitions.

This work represents the first investigation of integrating ultra-strong gradient dMRI with VERDICT modelling in the context of prostate cancer, thereby providing a novel contribution to the field. We designed deep learning models, including Multi-Layer Perceptron-based (MLP) and Convolutional Neural Networks-based (CNN) architectures, and performed comprehensive hyperparameter optimization to obtain the optimal configuration for ssVERDICT model fitting. We show that the self-supervised VERDICT model with a dense MLP architecture produces low-error, noise-free reconstructions of diffusion MRI signals, yielding accurate and stable parameter estimates that enhance tumour-normal tissue discrimination within regions of interest (ROI) compared to current clinical methods.

3 Materials and Methods

3.1 Data

3.1.1 Data Acquisition

Diffusion MRI was acquired on a Connectom research-only 3T MAGNETOM Skyra scanner (Siemens Healthcare, Erlangen, Germany) equipped with a 300 mT/m gradient coil [19]. A pulsed gradient spin echo (PGSE) with echo-planar imaging (EPI) sequence with six shells ($b = 0, 0.05, 0.5, 1.5, 2.0, 3.0$ ms/ μm^2) was used to acquire the data, each shell comprising 15 non-collinear directions with interspersed non-diffusion-weighted ($b = 0$) volumes. From this single acquisition, three sub-protocols were derived to emulate ultra-strong (300 mT/m) and clinical (80 and 40 mT/m) gradient systems, with corresponding minimum achievable $\text{TE}/\delta/\Delta$ [ms]: SP1 – 54/5/25, SP2 – 70/16/32, SP3 – 95/26/48, respectively, with TE, δ , and Δ held constant across all b-shells within each sub-protocol. Imaging parameters were consistent across sub-protocols: resolution = 1.3×1.3 mm², FOV = 220×220 mm², matrix = 168×168 , slice thickness = 5 mm, 14 slices, GRAPPA = 2, SMS = 2, partial Fourier = 6/8, bandwidth = 1860 Hz/pixel. Total scan time was approximately 20 min (6 min 35 sec per sub-protocol).

3.1.2 Patient Cohort

The dataset represents a subset of participants examined in [19], with the ethical approval for the study granted by the Cardiff University School of Psychology REC and the NHS REC (ref: 20/OCT/8264). This study included four healthy male volunteers (46–64 years; mean age = 54.8 ± 7.9 years) and five patients with histologically confirmed prostate adenocarcinoma enrolled in the Active Surveillance Programme (67–74 years; mean age = 69.8 ± 2.7 years). Cancer in the peripheral zone (PZ) was verified through elevated PSA levels, multiparametric MRI, and TRUS-guided biopsy, with Gleason scores of 3+3 or 3+4. Two of the five patients (hereafter labelled as PT 1, and PT 2) were assigned a Gleason score of 3+3, and the remaining three patients (hereafter labelled as PT 3 – PT 5) were assigned a score of 3+4. All participants underwent standard MRI safety checks and gave written informed consent.

3.1.3 ROI Delineation

Prostate masks were generated for all nine subjects using T2-weighted and $b = 0$ images. Radiologist confirmed tumour locations [18] were referenced for all patients. For each subject, the slice with the clearest conspicuity of the prostate and tumour ROI was manually delineated and approximated across the remaining slices due to the absence of full 3D masks. Boundaries around the gland were tightly drawn to limit surrounding voxels and reduce noise during model fitting.

3.1.4 Data Preprocessing

The pre-processing pipeline in [19] involved denoising [21], Gibbs ringing correction [22], partial distortion correction [23, 24], and adjustment of effective b-values and gradient directions [25], without eddy-current or motion correction. Subsequently, further preprocessing was performed on the dMRI data to enable training and inference with deep learning models. Diffusion-weighted images and b-vectors were loaded for each subject, with voxel-wise b-values computed as the Euclidean-norm of gradient components, averaged across voxels and slices, and assigned to the nearest theoretical value ($b = 0\text{--}3 \text{ ms}/\mu\text{m}^2$). For NLLS and MLP models, prostate masks were applied, spatial dimensions flattened, zero voxels discarded, repeated b-values averaged, and all signals normalized with b_0 (capped at 1), producing 2D arrays of [voxels \times b-values] concatenated across subjects. For CNNs, masks were omitted to preserve spatial uniformity. The images were kept at original resolution, averaged across identical b-values, normalized with b_0 , and permuted to [slices \times b-values \times image height \times image width].

3.1.5 Data Split

Each subject underwent a single dMRI acquisition from which three sub-protocols emulating high-performance and clinical gradient systems were derived. An identical pre-processing and data-splitting approach was applied across sub-protocols to maintain consistency in analysis. To emulate a clinical workflow, subjects were partitioned into three sets in chronological order of their acquisition date:

- Training Set: 2 healthy controls, 3 patients: PT 1 – PT 3
- Validation Set: 1 healthy control, 1 patient: PT 5
- Test Set: 1 healthy control, 1 patient: PT 4

These splits allowed assessment of training quality and evaluation on unseen data, ensuring the models learn meaningful mappings to estimate the parameters underlying the measured diffusion signals.

3.2 Diffusion MRI Models

3.2.1 Diffusion Kurtosis Imaging (DKI)

The scalar DKI formulation extends the mono-exponential ADC model with an additional second-order term accounting for non-Gaussian diffusion due to tissue heterogeneity and complexity. The normalized diffusion signal is defined as [26]:

$$\frac{S(b)}{S_0} = \exp\left(-bD_k + \frac{1}{6}b^2D_k^2K\right) \quad (3.1)$$

where b is the diffusion weighting (b-value), $S(b)$ and S_0 are signals at diffusion weighting b and zero respectively, D_k is the diffusivity and K is the excess kurtosis. Fitting the DKI model on the dMRI data requires the estimation of two parameters – D_k and K .

3.2.2 VERDICT

The VERDICT prostate framework can be formulated as the sum of diffusion signal contributions from intracellular (IC), extracellular-extravascular (EES), and vascular (VASC) compartments. The total normalized signal is given by [2, 11, 27]:

$$\frac{S}{S_0} = f_{ic}S_{ic}(d_{ic}, R, b, \Delta, \delta) + f_{ees}S_{ees}(d_{ees}, b) + f_{vasc}S_{vasc}(d_{vasc}, b) \quad (3.2)$$

where f_i , S_i , and d_i are the volume fractions, normalized diffusion signals, and diffusivities respectively in biophysical compartment i ($i = ic, ees$, or $vasc$); b is the diffusion weighting (b-value), S_0 is the signal at $b = 0$, R is the cell radius, Δ is the separation of the gradient pulse, and δ is the duration of the gradient pulse. Furthermore, the conditions $\sum_{i=1}^3 f_i = 1$ and $0 \leq f_i \leq 1$ allow us to compute f_{vasc} values directly from the values of f_{ic} and f_{ees} , given $f_{vasc} + f_{ic} + f_{ees} = 1$. In accordance with earlier studies [26], d_{ic} was set to $2 \mu\text{m}^2/\text{ms}$, while d_{vasc} was set to $8 \mu\text{m}^2/\text{ms}$. Therefore, the VERDICT framework requires estimation of four key microstructural parameters during model fitting [11, 27] – f_{ic} , f_{ees} , R , and d_{ees} .

3.3 Fitting Strategies

3.3.1 Non-linear least-squares (NLLS)

NLLS parameter estimation was performed using the LMFIT library in Python, which applies the Levenberg-Marquardt optimization algorithm, as in [2, 4, 26]. The objective function was defined as the difference between the measured diffusion signal and the model-predicted signal, and the sum of squared residuals (SSR) was minimized to obtain the model fitting. This yielded voxel-wise SSR values corresponding to the best-fit parameter estimates.

3.3.2 Deep Learning MLP: Baseline Architecture

The deep learning implementations in this study employed self-supervised autoencoder architecture with physics-informed decoder that minimizes the mean-squared error (MSE) between the normalized noisy measured MR signals ($S_{in} \rightarrow$ input data) and the normalized noise-free signals reconstructed from the estimated latent space parameters ($\hat{S}_{pred} \rightarrow$ output data). This implementation, hereafter referred to as Baseline MLP, derives its overall architecture from [11].

For both DKI and VERDICT, this model was implemented with an MLP encoder estimating the latent parameters and a decoder explicitly defined by the corresponding differentiable model equations (eq. 3.1 and 3.2). The encoder consisted of input layer of size 6 – each node corresponding to a distinct acquisition b-value – (0, 0.05, 0.5, 1.5, 2, 3) $\text{ms}/\mu\text{m}^2$. The encoder input layer is followed by three hidden layers with 10 neurons each and a latent output layer of size 2 for DKI, and size 4 for VERDICT. All hidden layers employed Parametric Rectified Linear Unit (PReLU) activations. To introduce stochastic regularization to mitigate overfitting, a dropout layer with rate $p = 0.2$ was applied immediately before the output layer.

To ensure non-negativity while preserving smooth gradient propagation, encoder outputs were passed through a Softplus activation and then clamped to physiologically plausible parameter-specific bounds.

The constrained parameters were then input to the decoder, to reconstruct biophysically meaningful, normalized, noise-free diffusion signals. The MSE between reconstructed and measured signals [12] served as the loss function. Training proceeded by minimizing this loss with the Adam optimizer, and gradient backpropagated end-to-end from the decoder to the encoder. The network employed the same hyperparameter configuration reported in [11], with a batch size of 256 and a constant learning rate of 0.001. A fixed number of epochs (60 for DKI; 300 for VERDICT) was set to systematically track training and validation loss and to assess the model convergence. These hyperparameters were applied uniformly across all three gradient strength datasets.

3.3.3 Deep Learning MLP: Dense and Improved Architecture

The Dense MLP extended the baseline architecture by deepening the encoder to maximize the model's ability to capture information from the six diffusion volumes. The latent space and the decoder remained unchanged. The encoder consisted of an input layer of 6 neurons followed by five hidden layers with 32, 64, 128, 64, and 32 neurons, respectively. This deeper design increased the model's representational capacity, raising the number of trainable VERDICT parameters from 337 (315 for DKI) in the baseline to 21,129 (21,063 for DKI) in the dense variant. PReLU activations and dropout layer were kept the same as in the baseline. Unlike the baseline, the dense model applied a Sigmoid activation at the encoder output to constrain parameters to $[0, 1]$, which were then linearly scaled to their biophysically realistic ranges. This approach preserved smooth gradient flow, in contrast to clamping, which can hinder gradients near the bounds. A schematic of the VERDICT dense MLP architecture is shown in Figure 1.

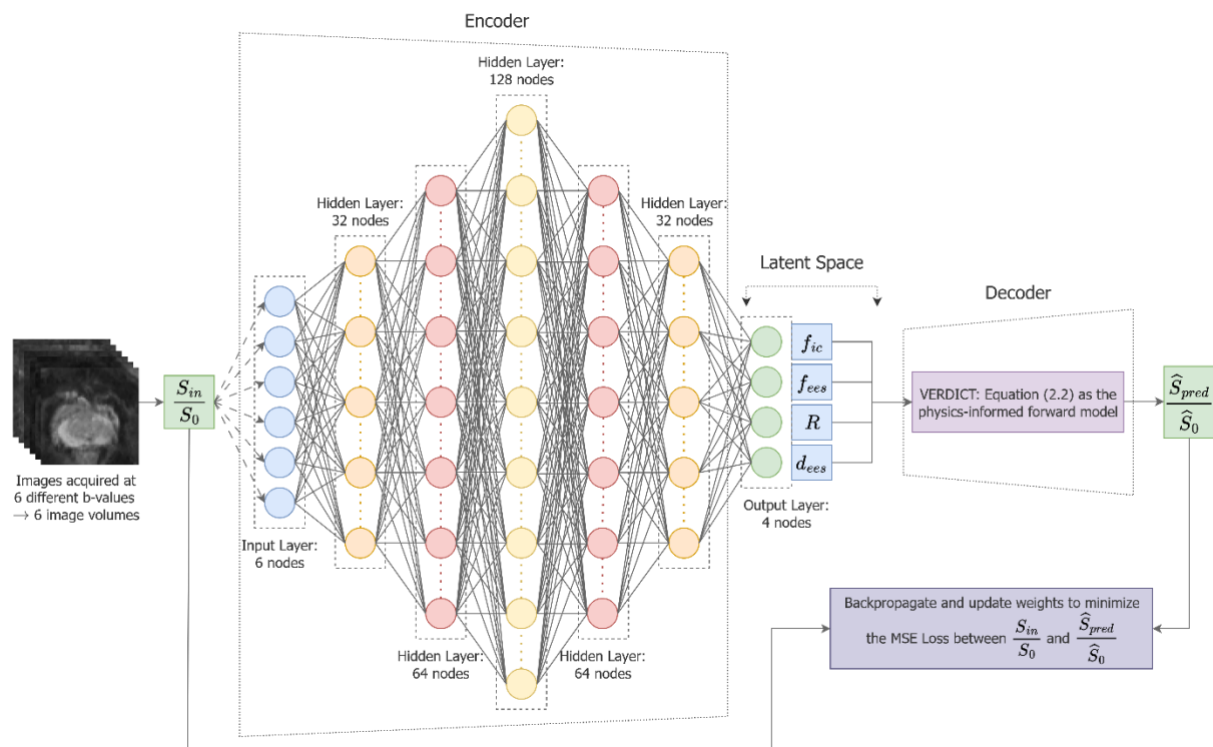


Figure 1: Schematic of VERDICT Dense MLP Architecture: The network takes six normalized diffusion signals as input, maps them to a four-node latent space representing VERDICT parameters, and passes these through a physics-informed decoder based on the VERDICT equations (eq. 3.2) to reconstruct the diffusion signal and minimize reconstruction error.

A full factorial grid search was performed over batch size (DKI $\in [32, 64, 128, 256]$; VERDICT $\in [64, 128, 256, 512]$) and initial learning rate ($[1e-4, 1e-3, 1e-2, 1e-1]$, common to both models), with tuning repeated independently for all three gradient strength datasets. The number of epochs was fixed at

60 and a learning rate scheduler reduced the initial learning rate by a factor of 0.1 every 10 epochs, enabling more precise weight updates and improved loss minimization. Table 1 lists the optimal hyperparameters identified for the DKI and VERDICT Dense MLP architectures.

3.3.4 Deep Learning CNN: U-Net Architecture

This procedure was not applied to DKI due to training instability with the available diffusion MRI data.

Within the similar physics-informed encoder-decoder framework, U-Net was added as an encoder with 6 input channels, each channel corresponding to a 2D image slice. The U-Net comprised a symmetric encoder-decoder structure with convolutional blocks and skip connections, compressing the input diffusion MRI slices to a 10×10 latent representation and progressively reconstructing them to the original 168×168 resolution [10, 15, 28]. The final 1×1 convolution mapped the 64-channel feature representation to the four VERDICT parameter maps, enabling spatially informed parameter estimation. This final convolution used a Sigmoid activation to constrain outputs to [0, 1], which were rescaled to physical ranges, flattened, and passed to the physics-informed VERDICT decoder to reconstruct the diffusion-weighted signals, with MSE minimized via Adam optimizer.

Unlike MLPs, the U-Net omitted prostate masks during preprocessing to maintain uniform image size, while applying the mask only during loss calculation so that gradient updates are restricted to prostate voxels. This avoids zero signal background bias, reduces zero-activation issues in PReLU layers, and improves both computational efficiency and convergence.

To ensure stable training with hyperparameter tuning, the U-Net batch size range was reduced, as channel-wise image processing in CNNs yields fewer effective training samples. A comprehensive grid search was performed over batch sizes of [1, 2, 5, 10], and initial learning rate of [1e-4, 1e-3, 1e-2, 1e-1]. The model was trained for 60 epochs at each iteration with a learning rate scheduler decreasing the initial value by a factor of 0.5 every 5 epochs. Table 1 also lists the optimal hyperparameter obtained for VERDICT U-Net.

Diffusion Models	Sub-Protocol (Gradient Strength)	Optimal Batch Size	Optimal Learning Rate (initial)
DKI: Dense MLP	SP1 (300 mT/m)	64	0.01
	SP2 (80 mT/m)	64	0.01
	SP3 (40 mT/m)	128	0.01
VERDICT: Dense MLP	SP1 (300 mT/m)	128	0.01
	SP2 (80 mT/m)	256	0.01
	SP3 (40 mT/m)	128	0.01
VERDICT: U-Net	SP1 (300 mT/m)	5	0.001
	SP2 (80 mT/m)	5	0.001
	SP3 (40 mT/m)	5	0.001

Table 1: Optimal hyperparameter configurations for Dense MLP (DKI and VERDICT) and U-Net (VERDICT) architecture across the three sub-protocols.

3.3.5 Evaluation Strategies and Metrics

For evaluating the quality of fit to the data with different models and fitting strategies, we computed the MSE between the normalized input and the noise-free reconstructed diffusion signals. To differentiate malignant from normal tissues, biomarker differences between paired tumour and normal ROIs (drawn from the same prostate) were tested for normality using the Shapiro-Wilk test, followed by a paired t-test or, if normality was violated, a Wilcoxon’s signed rank test.

We computed the mean biomarker value (K/f_{ic}) within the tumour ROI for each patient, and derived the Coefficient of Variation (CoV) as the ratio of standard deviation to the mean of these patient-level averages to assess inter-patient variability and model robustness. We additionally reported the pooled voxel-wise standard deviation of biomarker values across all patients to characterize voxel-level heterogeneity and instability (salt-and-pepper noise). Finally, we computed the CNR (median and inter-quartile range [IQR]) for each model across the patients to quantify lesion conspicuity relative to contralateral normal tissue, following the approach in [7, 29].

For Gleason grade discrimination, the independent samples (drawn from different prostates) were first tested for normality using Shapiro-Wilk test, and when violated, assessed for variance homogeneity (Levene's and Bartlett's tests). Accordingly, biomarker differences were then evaluated using the non-parametric Mann-Whitney U test.

4 Results

4.1 Model Evaluation

Figures 2 and 3 show the training and validation loss curves corresponding to optimal hyperparameter configurations for each model training process. All curves show clear evidence of stable convergence with VERDICT deep learning models saturating at lower MSE values than their DKI counterparts, with U-Net as an exception. Additionally, sub-protocol SP1 exhibits lower saturation MSE values than SP2 and SP3 for each fitting method.

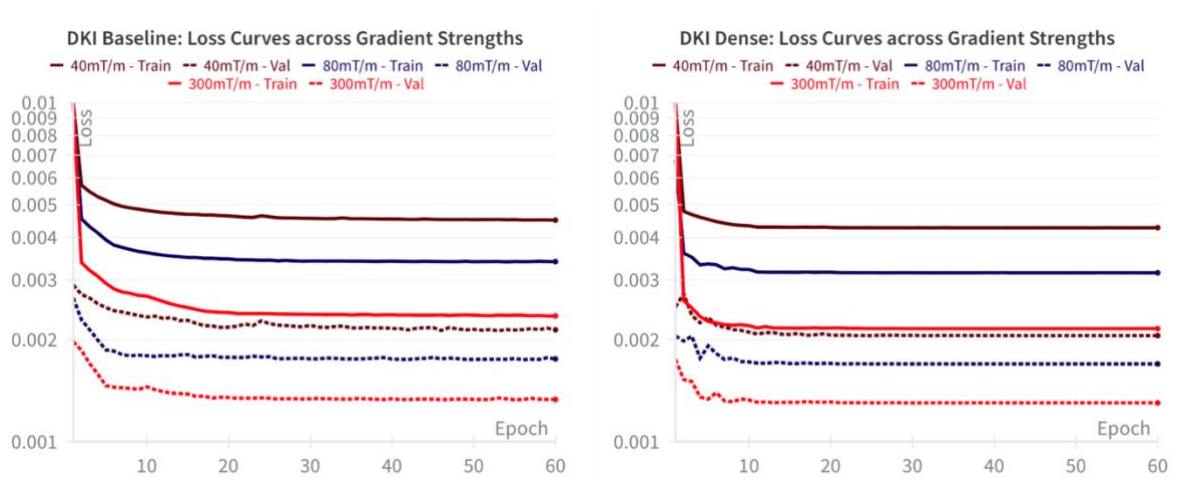


Figure 2: DKI Loss Curves: Training and Validation loss curves strengths for DKI Baseline MLP and Dense MLP models across three gradient sub-protocols. Both models show stable convergence, with Dense MLP consistently saturating at lower loss values than Baseline MLP. Loss increases with decreasing gradient strength, with SP1 (300 mT/m) yielding the lowest final MSE, followed by SP2 (80 mT/m) and SP3 (40 mT/m). Y-axis (Loss) is on the logarithmic scale.

Tables 2–4 provide a comparison of MSE values for patients and healthy controls on the held-out test set along with the validation and training losses at the best-performing epoch across SP1, SP2 and SP3 respectively. These results were obtained using model weights from the epoch with the lowest validation loss on the held-out test set.

Across all three sub-protocols, the VERDICT Dense MLP consistently achieved the lowest MSE among the deep learning models (Baseline MLP, Dense MLP, and U-Net) on the training and validation sets. Within the unseen test data, the best performing methods varied by subject with the VERDICT Dense MLP producing the lowest errors for the Healthy Control, and VERDICT NLLS achieving the lowest MSE

for Patient 4. These models marginally outperformed the next-best approaches across their respective cases in the test set.

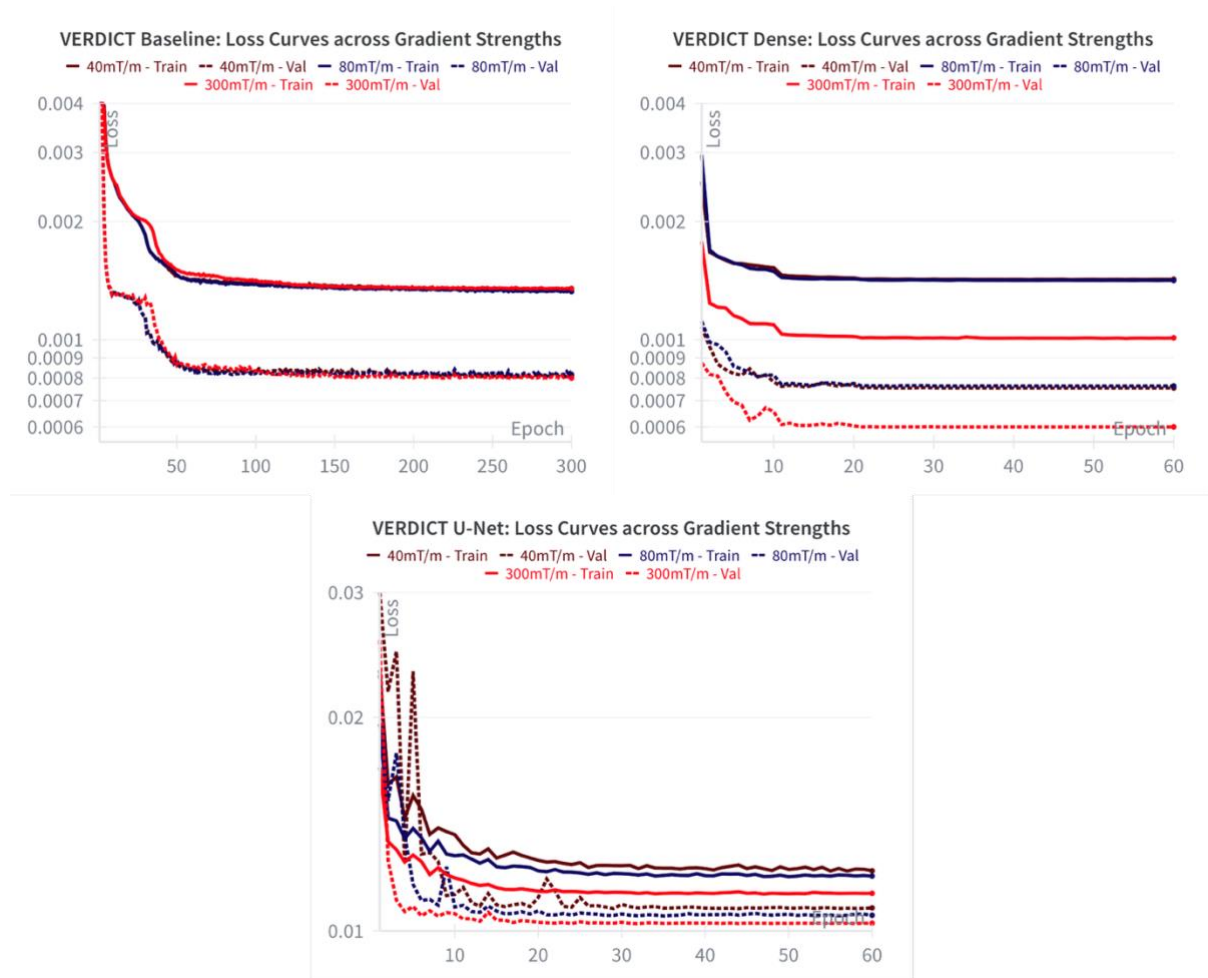


Figure 3: VERDICT Loss Curves: Training and Validation loss curves strengths for VERDICT Baseline MLP, Dense MLP, and U-Net models across three gradient sub-protocols. The Baseline MLP requires 300 epochs to converge, with losses nearly identical across SP1–SP3, reflecting limited representational capacity. Dense MLP and U-Net converge within 60 epochs. Dense MLP achieves lower loss, particularly for SP1, demonstrating improved learning and effective use of high-gradient data, while SP2 and SP3 remain slightly lower but still outperform Baseline MLP. Notably, U-Net exhibits higher losses relative to Baseline MLP and Dense MLP, though it still performs best on the ultra-strong gradient SP1 dataset relative to SP2 and SP3. Y-axis (Loss) is on the logarithmic scale.

Diffusion MRI Models	Fitting Models	Model Training			Model Inference	
		Best Val Epoch	Val Loss	Train Loss	Test Loss: Patient 4	Test Loss: Healthy
DKI	NLLS	—	—	—	6.71e-4	2.18e-3
	Baseline MLP	55	1.33e-3	2.36e-3	6.96e-4	2.25e-3
	Dense MLP	30	1.30e-3	2.15e-3	6.73e-4	2.21e-3
VERDICT	NLLS	—	—	—	2.62e-4	9.99e-4
	Baseline MLP	261 [#]	7.99e-4	1.35e-3	4.07e-4	1.12e-3
	Dense MLP	39	6.01e-4	1.01e-3	2.74e-4	9.73e-4
	U-Net	46	1.02e-2	1.13e-2	7.41e-3	3.02e-2

Table 2: SP1 (300 mT/m): Training, validation, and test losses across diffusion MRI models and fitting methods. On both the training and validation sets, VERDICT Dense MLP achieved the lowest reconstruction losses among the deep learning models. In the test set, VERDICT NLLS for Patient 4 and the VERDICT Dense MLP for the Healthy Control yielded the lowest losses, marginally outperforming the next-best models.

Diffusion MRI Models	Fitting Models	Model Training			Model Inference	
		Best Val Epoch	Val Loss	Train Loss	Test Loss: Patient 4	Test Loss: Healthy
DKI	NLLS	—	—	—	1.04e-3	2.97e-3
	Baseline MLP	56	1.74e-3	3.39e-3	1.11e-3	3.03e-3
	Dense MLP	30	1.69e-3	3.15e-3	1.04e-3	3.00e-3
VERDICT	NLLS	—	—	—	4.31e-4	1.24e-3
	Baseline MLP	205 [#]	9.65e-4	1.79e-3	5.97e-4	1.43e-3
	Dense MLP	28	7.63e-4	1.42e-3	4.49e-4	1.23e-3
	U-Net	46	1.05e-2	1.21e-2	7.84e-3	3.06e-2

Table 3: SP2 (80 mT/m): Training, validation, and test losses across diffusion MRI models and fitting methods. On both the training and validation sets, VERDICT Dense MLP achieved the lowest reconstruction losses among the deep learning models. In the test set, VERDICT NLLS for Patient 4 and the VERDICT Dense MLP for the Healthy Control yielded the lowest losses, marginally outperforming the next-best models.

Diffusion MRI Models	Fitting Models	Model Training			Model Inference	
		Best Val Epoch	Val Loss	Train Loss	Test Loss: Patient 4	Test Loss: Healthy
DKI	NLLS	—	—	—	3.18e-3	4.79e-3
	Baseline MLP	53	2.12e-3	4.52e-3	3.20e-3	4.87e-3
	Dense MLP	25	2.05e-3	4.28e-3	3.18e-3	4.82e-3
VERDICT	NLLS	—	—	—	2.05e-3	1.92e-3
	Baseline MLP	291 [#]	9.96e-4	1.91e-3	2.31e-3	2.13e-3
	Dense MLP	36	7.54e-4	1.44e-3	2.06e-3	1.92e-3
	U-Net	43	1.08e-2	1.23e-2	1.02e-2	3.16e-2

Table 4: SP3 (40 mT/m): Training, validation, and test losses across diffusion MRI models and fitting methods. On both the training and validation sets, VERDICT Dense MLP achieved the lowest reconstruction losses among the deep learning models. In the test set, VERDICT NLLS for Patient 4 and the VERDICT Dense MLP for the Healthy Control yielded the lowest losses, marginally outperforming the next-best models.

[#]: VERDICT Baseline MLP ran for 300 epochs unlike 60 for the other methods.

—: Fields that are not applicable for the NLLS method.

Table 5 summarises the Akaike Information Criterion corrected (AICc) and Bayesian Information Criterion (BIC) values and corresponding ranks for all diffusion MRI models and fitting strategies evaluated on the patient data in the test set (PT 4). Both criteria yielded an identical ordering of model performance, with VERDICT NLLS emerging as the best-fitting approach and the VERDICT Dense MLP ranking a close second. Across all comparisons, the VERDICT models performed better than the corresponding DKI models, indicating that the additional microstructural detail captured by VERDICT provides meaningful information rather than simply increasing the model complexity.

Models	AICc (* 10 ³)	Rank	BIC (* 10 ³)	Rank	No. of Parameters
VERDICT: NLLS	-68.542	1	-68.514	1	4
VERDICT: Dense MLP	-68.170	2	-68.142	2	4
VERDICT: Baseline MLP	-64.881	3	-64.853	3	4
DKI: NLLS	-60.729	4	-60.715	4	2
DKI: Dense MLP	-60.704	5	-60.690	5	2
DKI: Baseline MLP	-60.425	6	-60.411	6	2
VERDICT: U-Net	-40.761	7	-40.733	7	4

Table 5: SP1 (300 mT/m): AICc and BIC scores and ranks for different combinations of diffusion MRI models and fitting methods, evaluated on the Patient 4 from the test dataset. VERDICT NLLS marginally outperformed the VERDICT Dense MLP, achieving the best AICc and BIC ranks. Notably, the VERDICT models consistently outperformed their DKI counterparts.

4.2 Parameter Maps and Tumour-Normal Discrimination

All deep learning models were successfully trained with no evidence of overfitting, as demonstrated by the stable validation loss curves shown in Figures 2 and 3. This indicates that the models effectively approximated the inverse formulations of DKI and VERDICT, enabling inference on training and validation subject data to generate estimated parameter maps. In-vivo DKI and VERDICT parameter maps were generated for the five patients to qualitatively assess fitting quality and evaluate tumour ROI conspicuity, with two cases discussed below. Among these, the VERDICT intracellular volume fraction (f_{ic}) and DKI excess kurtosis (K) were obtained, both established as effective non-invasive biomarkers for cancer diagnosis [26, 30, 31].

Figure 4 illustrates the in vivo maps of fitted K and f_{ic} biomarkers for Patient 5. DKI maps showed little variability in visual quality across fitting methods, reflecting the model's low representational capacity and its ability to capture only limited tumour microstructural information. As a result, all fitting approaches converged to similar solutions regardless of complexity, unlike in VERDICT. VERDICT with Dense MLP and U-Net at 300 mT/m (SP1) exhibited superior lesion discrimination and fitting quality than SP2 and SP3, with SP3 performing worst. VERDICT NLLS maps remained uninformative, with multiple spurious highlighted regions reflecting the method's susceptibility to noise.

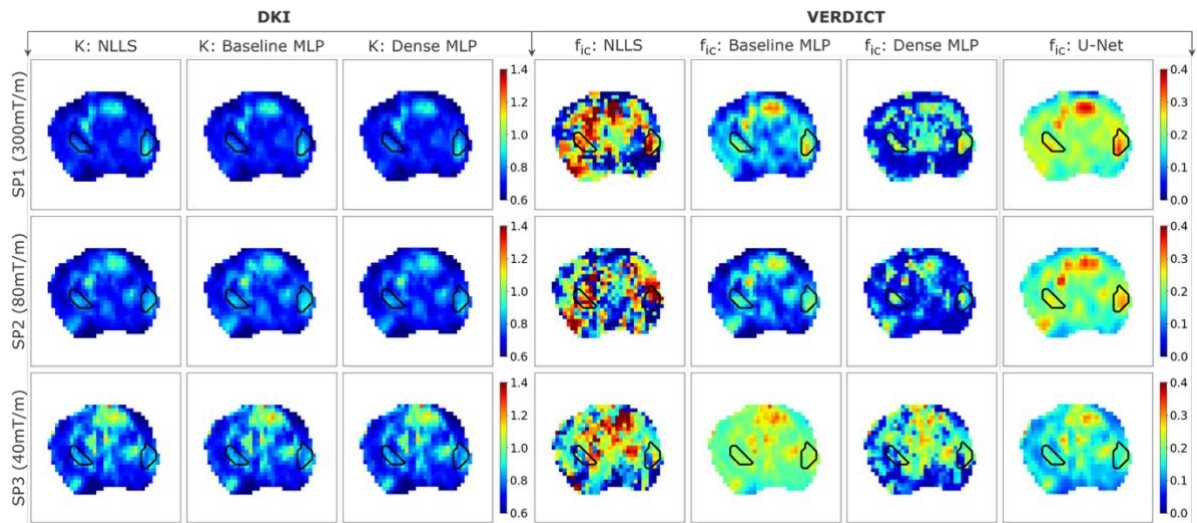


Figure 4: Comparison of K and f_{ic} parameter maps obtained using different fitting methods for both DKI and VERDICT models across the three sub-protocols for Patient 5. There are two 3+4 Gleason grade tumours present, one at left lateral PZ, and the other at right lateral PZ, both at mid-gland level. Deep learning methods (Baseline MLP, Dense MLP, U-Net) noticeably improve fitting over NLLS, with the best lesion conspicuity observed in SP1 at 300 mT/m. Dense MLP and U-Net slightly outperform Baseline MLP, while SP2 and SP3 remain suboptimal, underscoring the value of ultra-strong gradients for resolving tumour microstructure. For consistent visualization, K values are constrained to the interval [0.6, 1.4], and f_{ic} values are restricted to [0, 0.4], as indicated by the corresponding colorbars.

Figure 5 shows boxplots of the estimated K and f_{ic} distributions for Patient 5. All fitting methods distinguished malignant from normal tissue with strong statistical significance ($p < 0.001$) under SP1, while SP2 also showed separation but with weaker significance ($p < 0.05$) for some methods. SP3 performed worst, with median K and f_{ic} values exceeding those of lesions in some normal tissues, which is biophysically implausible. Despite the lesion's small size, SP1 reliably distinguished tumour from normal tissue, with narrower biomarker ranges.

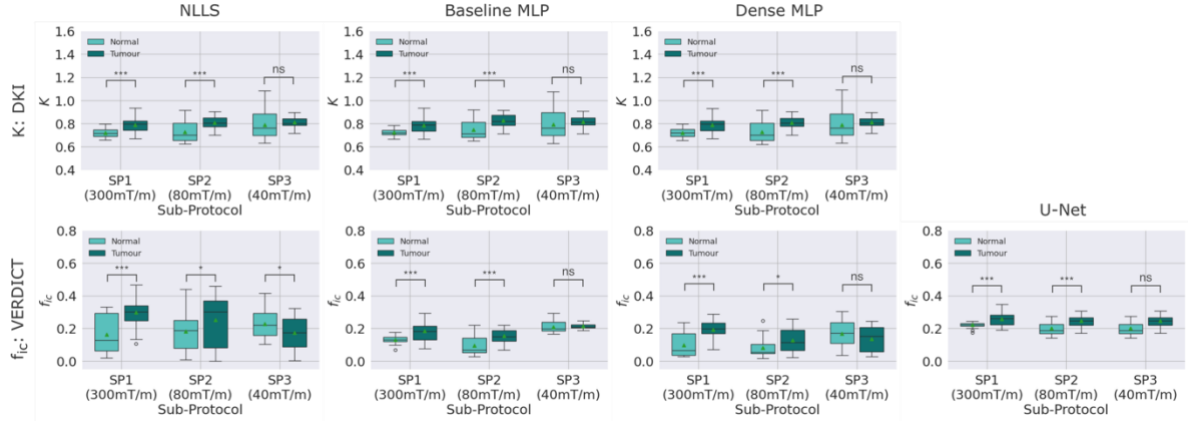


Figure 5: Boxplots illustrating the distributions of K and f_{ic} values across the three sub-protocols, compared across different fitting methods for both DKI and VERDICT models for Patient 5. In DKI, SP1 and SP2 significantly separate tumour and normal voxels, whereas SP3 fails, even producing implausible normal K values higher than the tumour K values. For VERDICT, SP1 yields strong tumour-normal separation across all methods ($p < 0.001$), SP2 shows weaker but significant differences, and SP3 performs poorly with physiologically unrealistic results for f_{ic} , just like DKI. To ensure consistency in visualization, the K values are constrained within the interval $[0.4, 1.6]$, while the f_{ic} values are restricted to $[0, 0.8]$. The following notation indicates statistical significance: *** $\rightarrow p < 0.001$; ** $\rightarrow p < 0.01$; * $\rightarrow p < 0.05$; and ns (non-significant) $\rightarrow p > 0.05$.

Figure 6 shows the estimated K and f_{ic} parameter maps for Patient 3. SP1 across all DKI fittings clearly highlighted both the lesions, but SP2 and SP3 showed reduced lesion conspicuity and ambiguous boundaries. VERDICT Baseline MLP, Dense MLP, and U-Net were able to effectively capture the lesion conspicuity with Dense MLP providing the best visual contrast. VERDICT NLLS maps were noisy and were barely able to capture the lesions boundaries. SP3 maps showed minimal discrimination and displayed artefacts in the upper right regions of the maps, pertaining to elevated levels of K and f_{ic} values that were unrelated to tumour.

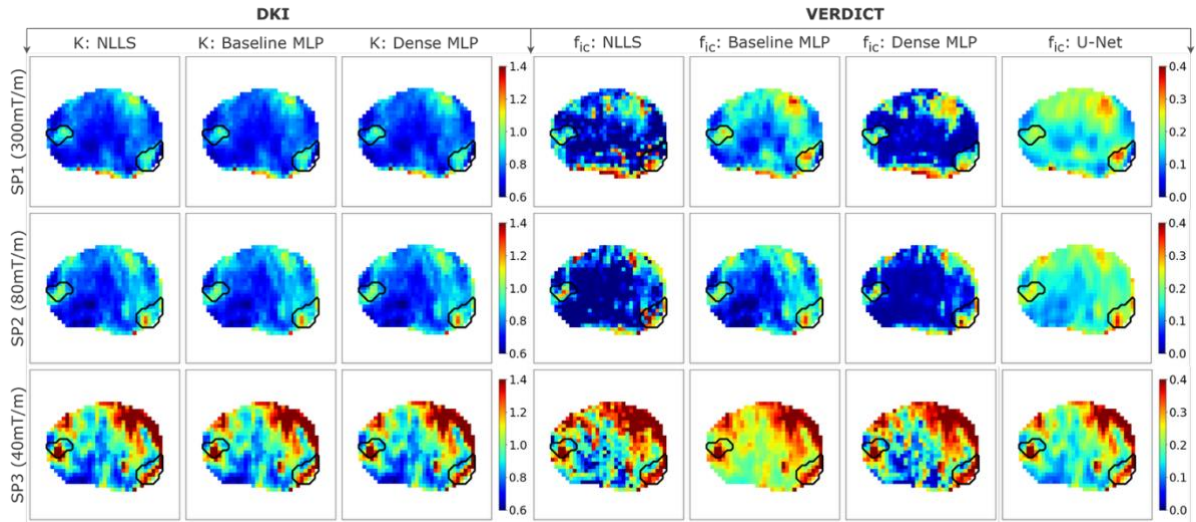


Figure 6: Comparison of K and f_{ic} parameter maps obtained using different fitting methods for both DKI and VERDICT models across the three sub-protocols for Patient 3. There are two 3+4 Gleason grade tumours present, one at left posterior and lateral PZ, and the other at right posterolateral PZ. Both tumours are well visualized in SP1 across DKI methods, but conspicuity diminishes in SP2 and SP3. VERDICT NLLS captures only the right lesion, whereas Baseline MLP, Dense MLP, and U-Net with strong gradients delineate both, with Dense MLP showing the best contrast. SP3 suffers from poor lesion visibility and artefacts, underscoring the limitations of low-gradient acquisitions (40 mT/m). For consistent visualization, K values are constrained to the interval $[0.6, 1.4]$, and f_{ic} values are restricted to $[0, 0.4]$, as indicated by the corresponding colorbars.

Figure 7 shows boxplots of the estimated K and f_{ic} distributions for Patient 3. Both DKI and VERDICT under SP1 and SP2 achieved strong separation between normal from tumour tissue ($p < 0.001$),

whereas SP3 showed relatively weaker differences ($p < 0.01$ for most methods, VERDICT NLLS $p < 0.05$). Overall, SP1 produced the most concentrated and biophysically plausible parameter distributions.

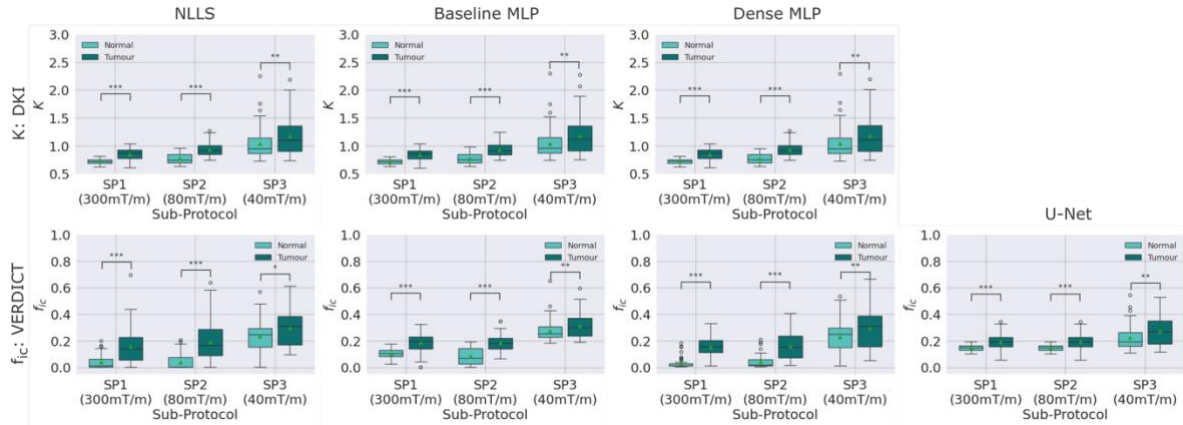


Figure 7: Boxplots illustrating the distributions of K and f_{ic} values across the three sub-protocols, compared across different fitting methods for both DKI and VERDICT models for Patient 3. For DKI, SP1 and SP2 produced strongly significant differences ($p < 0.001$) between tumour and normal K , while SP3 gave moderate separation ($p < 0.01$). For VERDICT, SP1 and SP2 achieved strong discrimination ($p < 0.001$) across all methods, whereas SP3 performed comparatively poorly, with weaker significance ($p < 0.05 - p < 0.01$). To ensure consistency in visualization, the K values are constrained within the interval $[0.5, 3.0]$, while the f_{ic} values are restricted to $[0, 1]$. The following notation indicates statistical significance: *** $\rightarrow p < 0.001$; ** $\rightarrow p < 0.01$; * $\rightarrow p < 0.05$; and ns (non-significant) $\rightarrow p > 0.05$.

Table 6 compares the CoV, pooled SD of tumour K and f_{ic} values, and the CNR between normal and cancerous lesions for the ultra-strong gradient data. Clear differences were observed across models, with the VERDICT Dense MLP showing the most consistent behaviour. It achieved lowest inter-patient CoV and the lowest pooled voxel-wise SD within tumour ROIs, indicating most stable and reliable parameter estimates. Additionally, it produced the highest CNR median with the most compact IQR, reflecting strongest separation between tumour and contralateral normal tissue. Overall, these results suggest that the VERDICT Dense MLP provides the most robust and discriminative biomarker estimates among the evaluated models.

Diffusion MRI Models	Fitting Models	Coefficient of Variation (CoV) (%)	Standard Deviation: Tumour ROI Biomarker (Pooled)	Contrast-to-Noise Ratio (CNR)	
				Median	IQR [Q1–Q3]
DKI (K)	NLLS	48.10%	7.87e-2	1.06	1.16 [0.94–2.21]
	Baseline MLP	48.87%	8.87e-2	1.10	1.33 [0.97–2.30]
	Dense MLP	48.30%	7.88e-2	1.08	1.33 [0.94–2.27]
VERDICT (f_{ic})	NLLS	43.76%	1.29e-1	1.17	0.70 [1.00–1.70]
	Baseline MLP	23.39%	6.85e-2	1.30	1.56 [1.00–2.56]
	Dense MLP	21.10%	6.48e-2	1.72	0.46 [1.40–1.86]
	U-Net	22.63%	6.91e-2	1.02	1.13 [0.87–2.00]

Table 6: SP1 (300 mT/m): Coefficient of Variation (CoV), pooled voxel-wise SD of tumour biomarker values, and CNR (median and IQR) between tumour and contralateral normal tissue across patient population for all diffusion MRI models and fitting methods. The VERDICT Dense MLP achieves the strongest overall performance, exhibiting the lowest CoV, the lowest pooled SD, and the highest median CNR with the most compact IQR.

We also assessed the parameter maps and biomarker distribution boxplots for patients 1, 2, and 4, with results demonstrated in Figures S1–S6. Additionally, we investigated whether any of the trained models, particularly VERDICT Dense MLP with access to ultra-strong gradient data, could meaningfully

discriminate between the two Gleason grade groups (3+3 and 3+4). The parameter maps and boxplots for these Gleason groups are illustrated in Figures S7–S8.

5 Discussion

This work presents first integration of ultra-strong gradient diffusion MRI with VERDICT modelling for prostate cancer, representing a novel step forward in the field. Previous studies using ultra-strong gradients have primarily employed mathematical models such as DKI [19] with conventional fitting approaches like NLLS, while VERDICT applications have so far been limited to clinical-strength systems [8, 11, 26, 31]. Our findings demonstrate that combining advanced acquisition with biophysical modelling enables new possibilities for non-invasive prostate tumour characterization.

We benchmarked DKI against VERDICT and compared multiple fitting strategies, including traditional NLLS, a baseline self-supervised MLP [11], a denser MLP extending the baseline, and a U-Net autoencoder. Our results show that VERDICT consistently outperformed DKI across all methods, with the Dense MLP and NLLS achieving the lowest reconstruction error in different cases on the ultra-strong gradient data (SP1). VERDICT NLLS also yielded the lowest MSE and the highest AICc and BIC rankings across individual patients (PT 1, PT 2, PT 4, and PT 5; Tables 2–4, S1). This marginally better MSE for NLLS is expected, as it is explicitly optimized to minimize the residual and, in doing so, overfits to the local noise. This is reflected in the noisier parameter maps in Figures 4 and 6, and the higher inter-patient variability (CoV) and pooled SD reported in Table 6. Interestingly, U-Net underperformed relative to Dense MLP, showing higher MSE values and notably lower AICc and BIC rankings, likely due to its higher data requirements. Importantly, ultra-strong gradients consistently reduced errors across sub-protocols, validating earlier findings that stronger diffusion gradients enhance sensitivity to restricted diffusion [20], and thereby improve characterization of intracellular, vascular, and extracellular-extravascular compartments.

In clinical practice, biomarkers reflecting tumour pathophysiology are vital for diagnosis and risk assessment, particularly in evaluating cancer grade and size. To capture these biomarkers non-invasively, we generated parameter heatmaps for K and f_{ic} across patients and estimation methods. Consistent with our hypothesis, VERDICT Dense MLP with ultra-strong gradient data (SP1) demonstrated high tumour-to-normal conspicuity, supported by the highest CNR (with narrowest IQR) reported in Table 6. This enabled clear delineation even in patients with small tumours or poorly defined lesion boundaries where traditional methods were less effective. On visual inspection, the VERDICT Dense MLP produced f_{ic} maps that were most anatomically similar to those from NLLS, but with notably reduced noise. U-Net achieved comparable visual performance, surpassing NLLS and Baseline MLP despite higher reconstruction losses, highlighting its ability to learn spatial microstructural features and its potential for further improvement with larger datasets.

Boxplot analysis of K and f_{ic} distributions showed that VERDICT Dense MLP under SP1 consistently delivered high level of statistical significance ($p < 0.001$) between tumour and normal tissues, particularly in cases with poor tumour conspicuity (PT 3 and PT 5). The U-Net outperformed both the NLLS and Baseline VERDICT models; however, distinguishing VERDICT from DKI remained challenging due to dataset limitations. Overall, the superior performance with SP1 underscores that ultra-strong gradients enhance sensitivity to cellular histology, enabling more reliable discrimination of tissue compartments. The enhanced lesion conspicuity and characterization achieved with VERDICT Dense MLP highlights its potential for integration with PI-RADS (Prostate Imaging Reporting and Data System)

in the current clinical systems for scoring of indeterminate lesions, suggesting it could improve non-invasive tumour assessment and reduce the need for biopsies [7, 11, 32].

Despite the demonstrated strengths of VERDICT Dense MLP with SP1, Gleason grade discrimination revealed a limitation. Ultra-strong gradients did not consistently distinguish grade 3+3 from 3+4, with SP1 occasionally estimating higher mean f_{ic} for 3+3, likely reflecting the small sample size rather than biological plausibility. Notably, SP3 (40 mT/m) showed the highest statistical significance in differentiating the grades among sub-protocols; however, this result is likely biased by the lower SNR at this gradient strength due to longer echo times [19] and should not be interpreted as a meaningful finding.

The main limitation of this study is the small cohort consisting of nine subjects that was not demographically matched due to limited sample size. Given that Black men in the UK have nearly twice the risk of developing prostate cancer compared to White men [33, 34], limited or non-representative training data may hinder model generalizability and introduce potential ethnicity-related bias. The limited sample size also contributed to higher reconstruction loss for U-Net with VERDICT and non-convergence of DKI training. Although the training and validation curves were generally stable, minor inconsistencies such as lower validation losses than training losses likely arose from patient-specific variability introduced by the small cohort and the data-split strategy.

Expanding this work to a larger and demographically diverse cohort in the future would be the most direct path to improve generalizability and robustness and to mitigate these limitations. Carefully incorporating data augmentation strategies could further enhance dataset diversity without compromising biophysical plausibility. With richer data, Vision Transformers (ViTs) [35] could be explored as a natural extension of the Dense MLP framework for more precise voxel-wise parameter estimation. Moreover, integrating relaxed-VERDICT (rVERDICT) [36] with ultra-strong gradient acquisitions could advance Gleason-grade discrimination, bringing this implementation closer to clinical translation. Advanced deep learning-based uncertainty estimation methods like Variational Autoencoders (VAEs) [37] and Bayesian Neural Networks [38] could be incorporated to provide deeper insights into the reliability and robustness of ultra-strong gradient acquisition systems, particularly under noisy conditions.

6 Conclusion

In conclusion, this study demonstrates that integrating ultra-strong gradient diffusion MRI with self-supervised VERDICT models, particularly the Dense MLP architecture, yield accurate, robust, consistent, and physiologically meaningful estimation of prostate microstructural parameters. Across patients and acquisition protocols, this approach outperformed conventional DKI and NLLS fitting methods, offering superior in vivo tumour-normal tissue discrimination and improved lesion conspicuity with highest CNR. Although Gleason grade differentiation was limited by the small cohort, these findings highlight the potential of combining high-quality diffusion data with advanced deep learning to enhance non-invasive tumour characterization and reduce the need for unnecessary biopsies.

7 References

1. Bray, F., Laversanne, M., Sung, H., Ferlay, J., Siegel, R. L., Soerjomataram, I., & Jemal, A. (2024). Global cancer statistics 2022: GLOBOCAN estimates of incidence and mortality worldwide for 36 cancers in 185 countries. *CA: a cancer journal for clinicians*, 74(3), 229-263.
2. Panagiotaki, E., Walker-Samuel, S., Siow, B., Johnson, S. P., Rajkumar, V., Pedley, R. B., ... & Alexander, D. C. (2014). Noninvasive quantification of solid tumor microstructure using VERDICT MRI. *Cancer research*, 74(7), 1902-1912.
3. Afaq, A., Andreou, A., & Koh, D. M. (2010). Diffusion-weighted magnetic resonance imaging for tumour response assessment: why, when and how?. *Cancer imaging*, 10(1A), S179.
4. Le Bihan, D., Breton, E., Lallemand, D., Grenier, P., Cabanis, E., & Laval-Jeantet, M. (1986). MR imaging of intravoxel incoherent motions: application to diffusion and perfusion in neurologic disorders. *Radiology*, 161(2), 401-407.
5. Jensen, J. H., Helpert, J. A., Ramani, A., Lu, H., & Kaczynski, K. (2005). Diffusional kurtosis imaging: the quantification of non-gaussian water diffusion by means of magnetic resonance imaging. *Magnetic Resonance in Medicine: An Official Journal of the International Society for Magnetic Resonance in Medicine*, 53(6), 1432-1440.
6. Panagiotaki, E., Schneider, T., Siow, B., Hall, M. G., Lythgoe, M. F., & Alexander, D. C. (2012). Compartment models of the diffusion MR signal in brain white matter: a taxonomy and comparison. *Neuroimage*, 59(3), 2241-2254.
7. Johnston, E. W., Bonet-Carne, E., Ferizi, U., Yvernault, B., Pye, H., Patel, D., ... & Punwani, S. (2019). VERDICT MRI for prostate cancer: intracellular volume fraction versus apparent diffusion coefficient. *Radiology*, 291(2), 391-397.
8. Bailey, C., Bourne, R. M., Siow, B., Johnston, E. W., Brizmohun Appayya, M., Pye, H., ... & Panagiotaki, E. (2019). VERDICT MRI validation in fresh and fixed prostate specimens using patient-specific moulds for histological and MR alignment. *NMR in Biomedicine*, 32(5), e4073.
9. Bourne, R. M., Panagiotaki, E., Bongers, A., Sved, P., Watson, G., & Alexander, D. C. (2014). Information theoretic ranking of four models of diffusion attenuation in fresh and fixed prostate tissue ex vivo. *Magnetic resonance in medicine*, 72(5), 1418-1426.
10. Vasylechko, S. D., Warfield, S. K., Afacan, O., & Kurugol, S. (2022). Self-supervised IVIM DWI parameter estimation with a physics based forward model. *Magnetic resonance in medicine*, 87(2), 904-914.
11. Sen, S., Singh, S., Pye, H., Moore, C. M., Whitaker, H. C., Punwani, S., ... & Sator, P. J. (2024). ssVERDICT: Self-supervised VERDICT-MRI for enhanced prostate tumor characterization. *Magnetic resonance in medicine*, 92(5), 2181-2192.
12. Barbieri, S., Gurney-Champion, O. J., Klaassen, R., & Thoeny, H. C. (2020). Deep learning how to fit an intravoxel incoherent motion model to diffusion-weighted MRI. *Magnetic resonance in medicine*, 83(1), 312-321.
13. Gyori, N. G., Palombo, M., Clark, C. A., Zhang, H., & Alexander, D. C. (2022). Training data distribution significantly impacts the estimation of tissue microstructure with machine learning. *Magnetic resonance in medicine*, 87(2), 932-947.
14. Epstein, S. C., Bray, T. J., Hall-Craggs, M., & Zhang, H. (2022). Choice of training label matters: how to best use deep learning for quantitative MRI parameter estimation. *arXiv preprint arXiv:2205.05587*.
15. Huang, H. M. (2022). An unsupervised convolutional neural network method for estimation of intravoxel incoherent motion parameters. *Physics in Medicine & Biology*, 67(21), 215018.
16. Voorter, P. H., Backes, W. H., Gurney-Champion, O. J., Wong, S. M., Staals, J., van Oostenbrugge, R. J., ... & Drenthen, G. S. (2023). Improving microstructural integrity, interstitial fluid, and blood

microcirculation images from multi-b-value diffusion MRI using physics-informed neural networks in cerebrovascular disease. *Magnetic Resonance in Medicine*, 90(4), 1657-1671.

17. Raissi, M., Perdikaris, P., & Karniadakis, G. E. (2019). Physics-informed neural networks: A deep learning framework for solving forward and inverse problems involving nonlinear partial differential equations. *Journal of Computational physics*, 378, 686-707.
18. Karniadakis, G. E., Kevrekidis, I. G., Lu, L., Perdikaris, P., Wang, S., & Yang, L. (2021). Physics-informed machine learning. *Nature Reviews Physics*, 3(6), 422-440.
19. Molendowska, M., Palombo, M., Foley, K. G., Narahari, K., Fasano, F., Jones, D. K., ... & Tax, C. M. (2024). Diffusion MRI in prostate cancer with ultra-strong whole-body gradients. *NMR in Biomedicine*, 37(12), e5229.
20. Jones, D. K., Alexander, D. C., Bowtell, R., Cercignani, M., Dell'Acqua, F., McHugh, D. J., ... & Tax, C. M. (2018). Microstructural imaging of the human brain with a 'super-scanner': 10 key advantages of ultra-strong gradients for diffusion MRI. *NeuroImage*, 182, 8-38.
21. Cordero-Grande, L., Christiaens, D., Hutter, J., Price, A. N., & Hajnal, J. V. (2019). Complex diffusion-weighted image estimation via matrix recovery under general noise models. *Neuroimage*, 200, 391-404.
22. Lee, H. H., Novikov, D. S., & Fieremans, E. (2021). Removal of partial Fourier-induced Gibbs (RPG) ringing artifacts in MRI. *Magnetic resonance in medicine*, 86(5), 2733-2750.
23. Andersson, J. L., Skare, S., & Ashburner, J. (2003). How to correct susceptibility distortions in spin-echo echo-planar images: application to diffusion tensor imaging. *Neuroimage*, 20(2), 870-888.
24. Jovicich, J., Czanner, S., Greve, D., Haley, E., van Der Kouwe, A., Gollub, R., ... & Dale, A. (2006). Reliability in multi-site structural MRI studies: effects of gradient non-linearity correction on phantom and human data. *Neuroimage*, 30(2), 436-443.
25. Bammer, R., Markl, M., Barnett, A., Acar, B., Alley, M. T., Pelc, N. J., ... & Moseley, M. E. (2003). Analysis and generalized correction of the effect of spatial gradient field distortions in diffusion-weighted imaging. *Magnetic Resonance in Medicine: An Official Journal of the International Society for Magnetic Resonance in Medicine*, 50(3), 560-569.
26. Panagiotaki, E., Chan, R. W., Dikaio, N., Ahmed, H. U., O'Callaghan, J., Freeman, A., ... & Alexander, D. C. (2015). Microstructural characterization of normal and malignant human prostate tissue with vascular, extracellular, and restricted diffusion for cytometry in tumours magnetic resonance imaging. *Investigative radiology*, 50(4), 218-227.
27. Bonet-Carne, E., Johnston, E., Daducci, A., Jacobs, J. G., Freeman, A., Atkinson, D., ... & Panagiotaki, E. (2019). VERDICT-AMICO: Ultrafast fitting algorithm for non-invasive prostate microstructure characterization. *NMR in Biomedicine*, 32(1), e4019.
28. Ronneberger, O., Fischer, P., & Brox, T. (2015, October). U-net: Convolutional networks for biomedical image segmentation. In *International Conference on Medical image computing and computer-assisted intervention* (pp. 234-241). Cham: Springer international publishing.
29. Grussu, F., Schneider, T., Zhang, H., Alexander, D. C., & Wheeler-Kingshott, C. A. (2015). Neurite orientation dispersion and density imaging of the healthy cervical spinal cord in vivo. *Neuroimage*, 111, 590-601.
30. Tamura, C., Shinmoto, H., Soga, S., Okamura, T., Sato, H., Okuaki, T., ... & Kaji, T. (2014). Diffusion kurtosis imaging study of prostate cancer: preliminary findings. *Journal of magnetic resonance imaging*, 40(3), 723-729.
31. Singh, S., Rogers, H., Kanber, B., Clemente, J., Pye, H., Johnston, E. W., ... & Punwani, S. (2022). Avoiding unnecessary biopsy after multiparametric prostate MRI with VERDICT analysis: the INNOVATE study. *Radiology*, 305(3), 623-630.

32. Turkbey, B., Rosenkrantz, A. B., Haider, M. A., Padhani, A. R., Villeirs, G., Macura, K. J., ... & Weinreb, J. C. (2019). Prostate imaging reporting and data system version 2.1: 2019 update of prostate imaging reporting and data system version 2. *European urology*, 76(3), 340-351.
33. Lloyd, T., Hounscome, L., Mehay, A., Mee, S., Verne, J., & Cooper, A. (2015). Lifetime risk of being diagnosed with, or dying from, prostate cancer by major ethnic group in England 2008–2010. *BMC medicine*, 13(1), 171.
34. Bokhorst, L. P., & Roobol, M. J. (2015). Ethnicity and prostate cancer: the way to solve the screening problem?. *BMC medicine*, 13(1), 179.
35. Zheng, T., Yan, G., Li, H., Zheng, W., Shi, W., Zhang, Y., ... & Wu, D. (2023). A microstructure estimation Transformer inspired by sparse representation for diffusion MRI. *Medical Image Analysis*, 86, 102788.
36. Palombo, M., Valindria, V., Singh, S., Chiou, E., Giganti, F., Pye, H., ... & Panagiotaki, E. (2023). Joint estimation of relaxation and diffusion tissue parameters for prostate cancer with relaxation-VERDICT MRI. *Scientific Reports*, 13(1), 2999.
37. Xu, M., Zhou, Y., Goodwin-Allcock, T., Firoozabadi, K., Jacob, J., Alexander, D. C., & Sator, P. J. (2024). MRI Parameter Mapping via Gaussian Mixture VAE: Breaking the Assumption of Independent Pixels. *arXiv preprint arXiv:2411.10772*.
38. Jallais, M., & Palombo, M. (2024). Introducing μ GUIDE for quantitative imaging via generalized uncertainty-driven inference using deep learning. *Elife*, 13, RP101069.

8 Supplementary Information

Diffusion MRI Models	Fitting Models	Patient-wise MSE			
		Patient 1	Patient 2	Patient 3	Patient 5
DKI	NLLS	1.91e-3	2.29e-3	2.37e-3	8.23e-4
	Baseline MLP	1.96e-3	2.37e-3	2.41e-3	9.32e-4
	Dense MLP	1.92e-3	2.30e-3	2.37e-3	9.06e-4
VERDICT	NLLS	7.46e-4	9.33e-4	1.23e-3	3.76e-4
	Baseline MLP	9.13e-4	1.16e-3	1.38e-3	5.24e-4
	Dense MLP	7.49e-4	9.53e-4	1.20e-3	3.87e-4
	U-Net	2.49e-2	7.06e-3	3.64e-3	6.49e-4

Table S1: SP1 (300 mT/m): Reconstruction MSE across diffusion MRI models and fitting methods for individual patients under ultra-strong gradients. Patient 4 results are reported in Tables 2–4. VERDICT NLLS yielded the lowest losses for Patients 1, 2 and 5, while VERDICT Dense MLP preformed best for Patient 3. In all cases, these methods only marginally outperformed their next-best approaches.

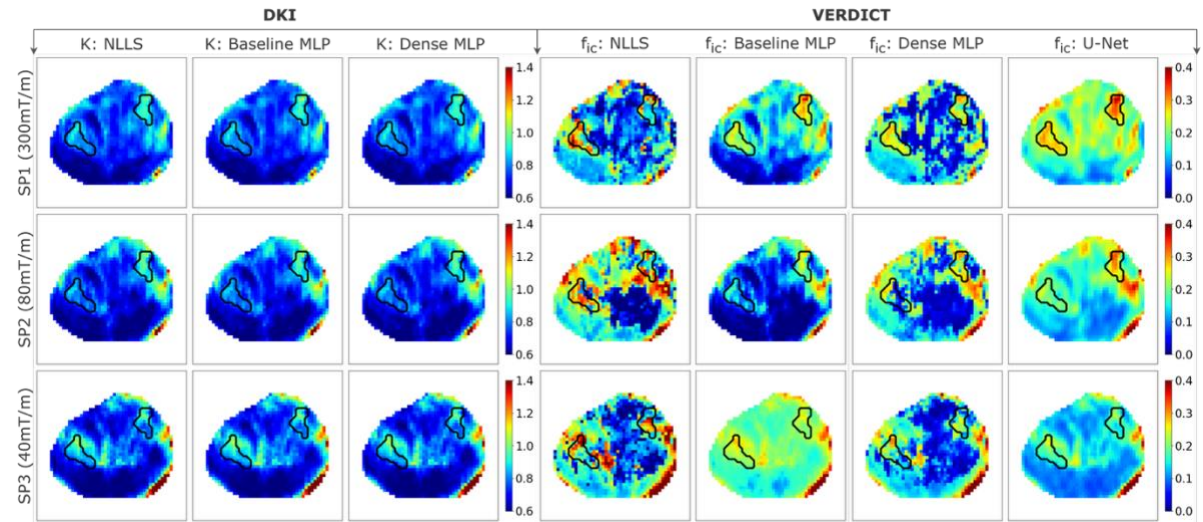


Figure S1: Comparison of K and f_{ic} parameter maps obtained using different fitting methods for both DKI and VERDICT models across the three sub-protocols for Patient 1. Two 3+3 grade lesions are present: one at right posterolateral PZ and another at left anterior PZ, both at the apex. At 300 mT/m (SP1), VERDICT Baseline MLP, Dense MLP, and U-Net methods yield clear lesion delineation, whereas DKI and VERDICT NLLS remain less informative. The U-Net f_{ic} map offers sharper delineation of the left anterior PZ tumour, whereas Dense MLP delineates right posterolateral PZ tumour with higher conspicuity. Lesion contrast diminishes in SP2 and SP3. For consistent visualization, K values are constrained to the interval [0.6, 1.4], and f_{ic} values are restricted to [0, 0.4], as indicated by the corresponding colorbars.

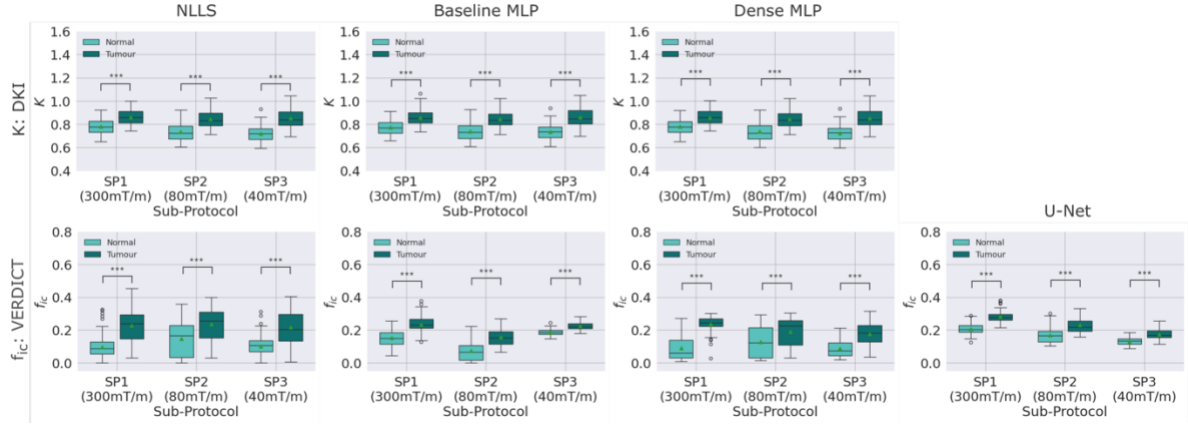


Figure S2: Boxplots illustrating the distributions of K and f_{ic} values across the three sub-protocols, compared across different fitting methods for both DKI and VERDICT models for Patient 1. All DKI fitting methods show strong tumour-normal separation ($p < 0.001$). VERDICT similarly yields strong statistical difference ($p < 0.001$), with SP1 producing the narrowest distributions and clearest separation. To ensure consistency in visualization, the K values are constrained within the interval $[0.5, 3.0]$, while the f_{ic} values are restricted to $[0, 1]$. The following notation indicates statistical significance: *** $\rightarrow p < 0.001$; ** $\rightarrow p < 0.01$; * $\rightarrow p < 0.05$; and ns (non-significant) $\rightarrow p > 0.05$.

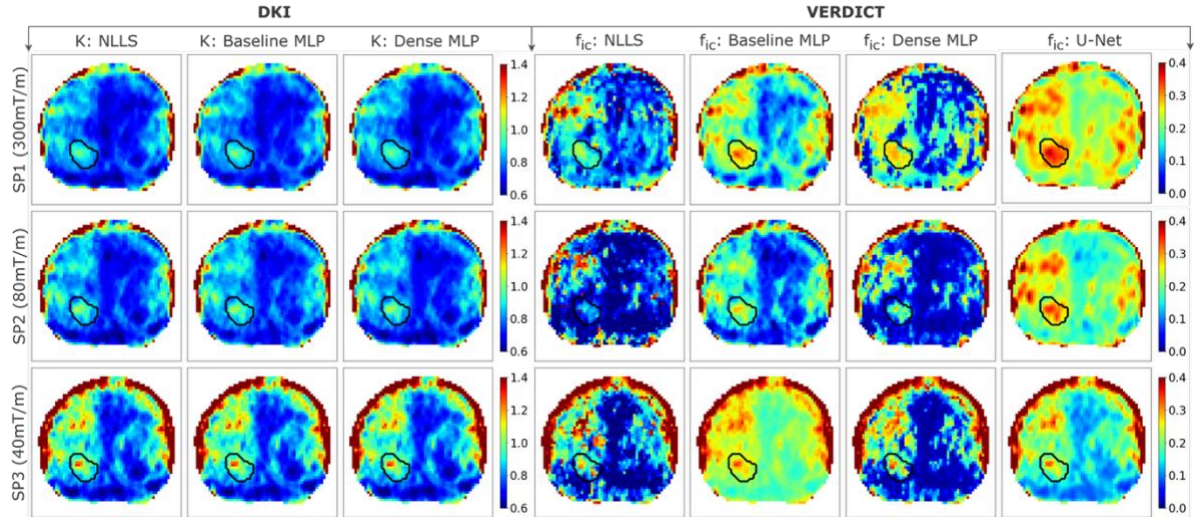


Figure S3: Comparison of K and f_{ic} parameter maps obtained using different fitting methods for both DKI and VERDICT models across the three sub-protocols for Patient 2. A lesion of grade 3+3 is present at the right posterolateral PZ at the base. DKI K maps under SP1 provide superior lesion discrimination. The tumour is best captured by U-Net, followed by Dense and Baseline MLPs. Lesion visibility persists at SP2 for Dense MLP and U-Net but is lost at SP3. For consistent visualization, K values are constrained to the interval $[0.6, 1.4]$, and f_{ic} values are restricted to $[0, 0.4]$, as indicated by the corresponding colorbars.

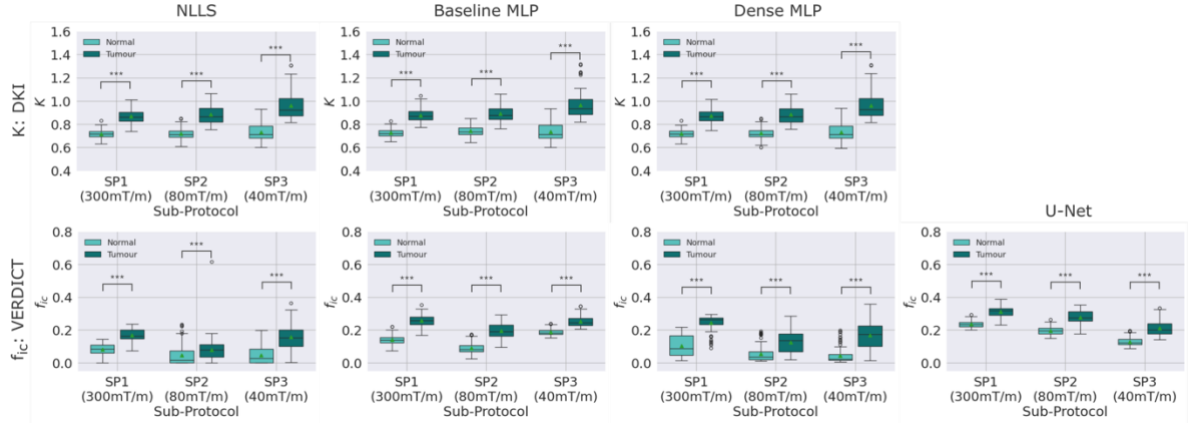


Figure S4: Boxplots illustrating the distributions of K and f_{ic} values across the three sub-protocols, compared across different fitting methods for both DKI and VERDICT models for Patient 2. DKI shows consistent tumour-normal separation across fitting methods and protocols. VERDICT NLLS yields near-zero f_{ic} in SP2 and SP3 but not in SP1. All VERDICT methods achieved significant tumour-normal separation ($p < 0.001$), with SP1 showing the most concentrated distributions. To ensure consistency in visualization, the K values are constrained within the interval $[0.5, 3.0]$, while the f_{ic} values are restricted to $[0, 1]$. The following notation indicates statistical significance: *** $\rightarrow p < 0.001$; ** $\rightarrow p < 0.01$; * $\rightarrow p < 0.05$; and ns (non-significant) $\rightarrow p > 0.05$.

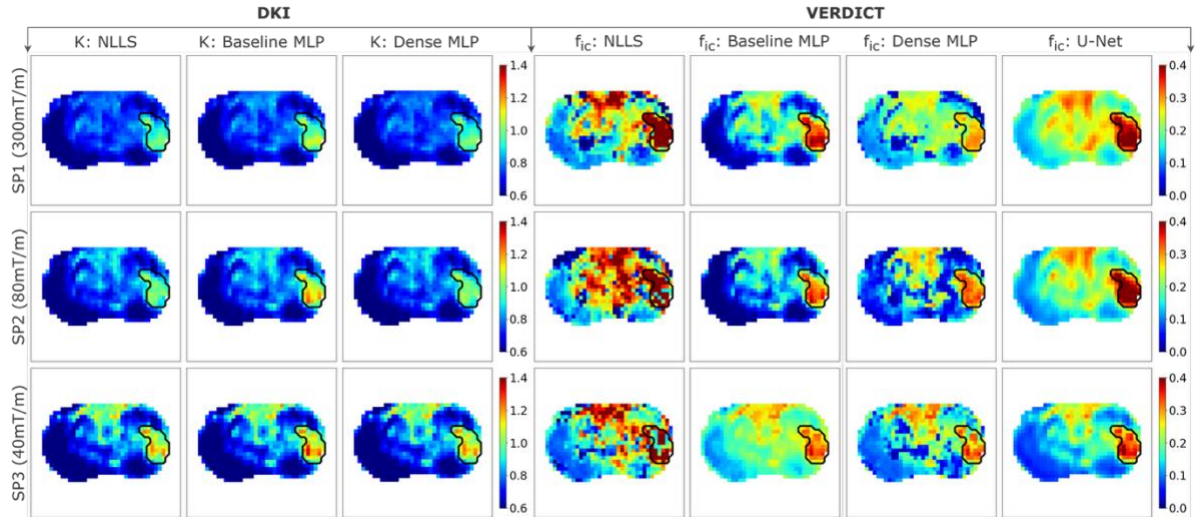


Figure S5: Comparison of K and f_{ic} parameter maps obtained using different fitting methods for both DKI and VERDICT models across the three sub-protocols for Patient 4. A lesion of grade 3+4 is present at the left PZ at the base and mid-gland. All maps show clear tumour conspicuity. DKI maps appear similar across fitting methods, while VERDICT NLLS maps are noisy and U-Net produces the smoothest outputs. The VERDICT Baseline MLP underperforms due to f_{ic} saturation near zero. SP1 and SP2 enable stronger lesion discrimination than SP3, with SP1 performing best. For consistent visualization, K values are constrained to the interval $[0.6, 1.4]$, and f_{ic} values are restricted to $[0, 0.4]$, as indicated by the corresponding colorbars.

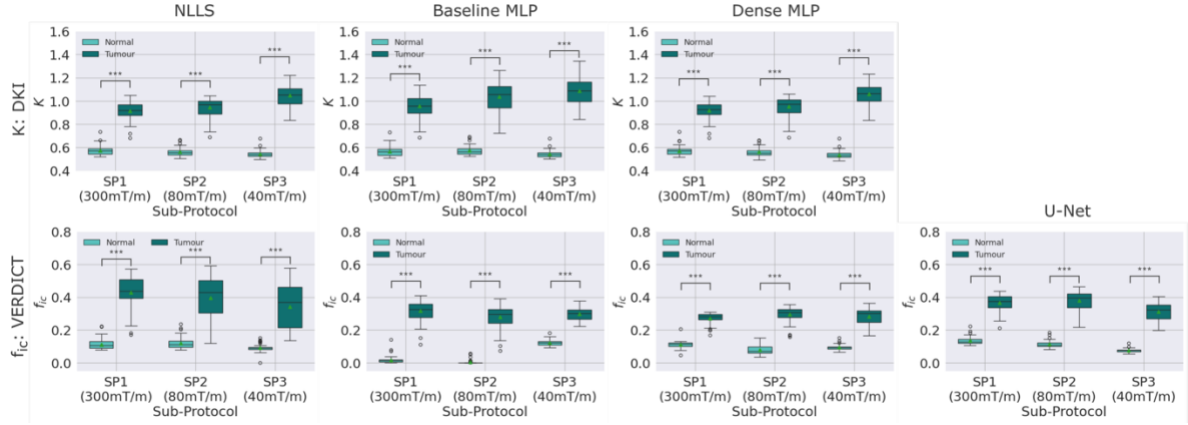


Figure S6: Boxplots illustrating the distributions of K and f_{ic} values across the three sub-protocols, compared across different fitting methods for both DKI and VERDICT models for Patient 4. Both DKI and VERDICT show highly significant differences between tumour and normal regions ($p < 0.001$). VERDICT Baseline MLP produces implausible near-zero f_{ic} estimates in normal ROIs, corrected by NLLS, Dense MLP, and U-Net. SP1 (300 mT/m) yields the most concentrated distributions. To ensure consistency in visualization, the K values are constrained within the interval $[0.5, 3.0]$, while the f_{ic} values are restricted to $[0, 1]$. The following notation indicates statistical significance: *** $\rightarrow p < 0.001$; ** $\rightarrow p < 0.01$; * $\rightarrow p < 0.05$; and ns (non-significant) $\rightarrow p > 0.05$.

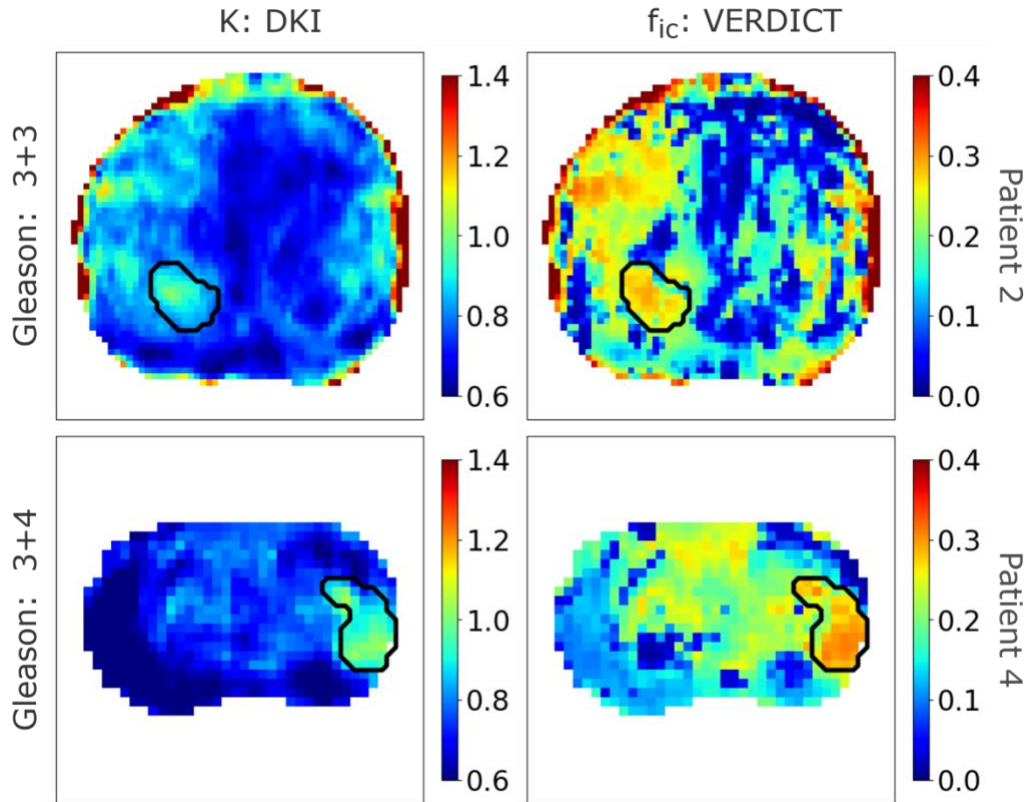


Figure S7: Comparison of tumour-to-normal tissue contrast in the K and f_{ic} parameter maps derived from DKI and VERDICT models for two representative patients: Patient 2, assigned Gleason grade 3+3, and Patient 4, assigned Gleason grade 3+4. Both models were fitted using the dense MLP approach to ensure consistency in the comparison. For consistent visualization, K values are constrained to the interval $[0.6, 1.4]$, and f_{ic} values are restricted to $[0, 0.4]$, as indicated by the corresponding colorbars.

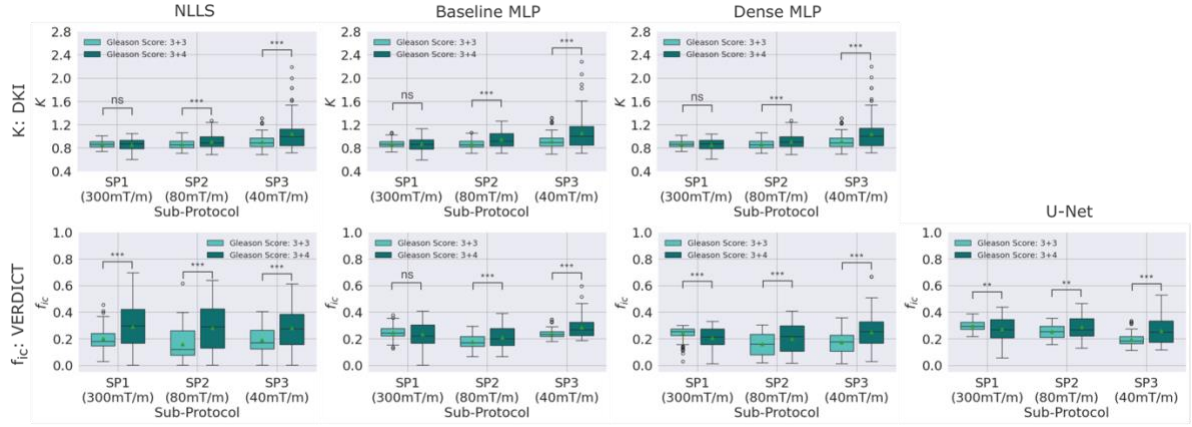


Figure S8: Boxplots illustrating the distributions of K and f_{ic} values across the three sub-protocols for Gleason scores 3+3 and 3+4, compared across different fitting methods for both DK1 and VERDICT models. SP1 failed to distinguish grades in DK1 and VERDICT Baseline MLP, while SP2 and SP3 achieved strong significance ($p < 0.001$). Dense MLP achieved significant separation across all protocols, though SP1 occasionally overestimated f_{ic} in Gleason 3+3, contrary to histological expectations. Unexpectedly, SP3 provided the statistically highest Gleason-grade discrimination, and is likely a biased result due to low SNR. To ensure consistency in visualization, the K values are constrained within the interval $[0.4, 2.8]$, while the f_{ic} values are restricted to $[0, 1]$. The following notation indicates statistical significance: *** $\rightarrow p < 0.001$; ** $\rightarrow p < 0.01$; * $\rightarrow p < 0.05$; and ns (non-significant) $\rightarrow p > 0.05$.

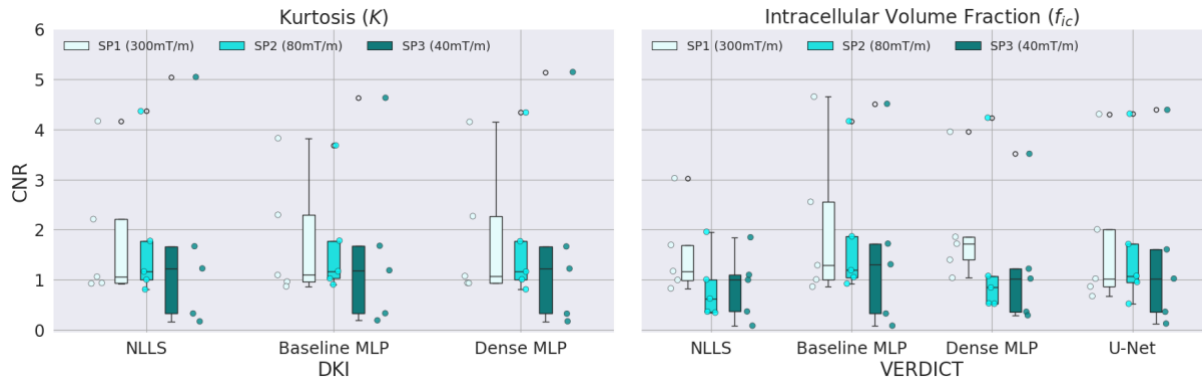


Figure S9: Boxplots showing CNR values across the three sub-protocols for different fitting methods for both DK1 and VERDICT models. Across all models and methods, VERDICT Dense MLP under SP1 (300 mT/m) achieved the highest median CNR and the narrowest inter-quartile range (IQR).

SP1 (300mT/m): Patients Aggregated

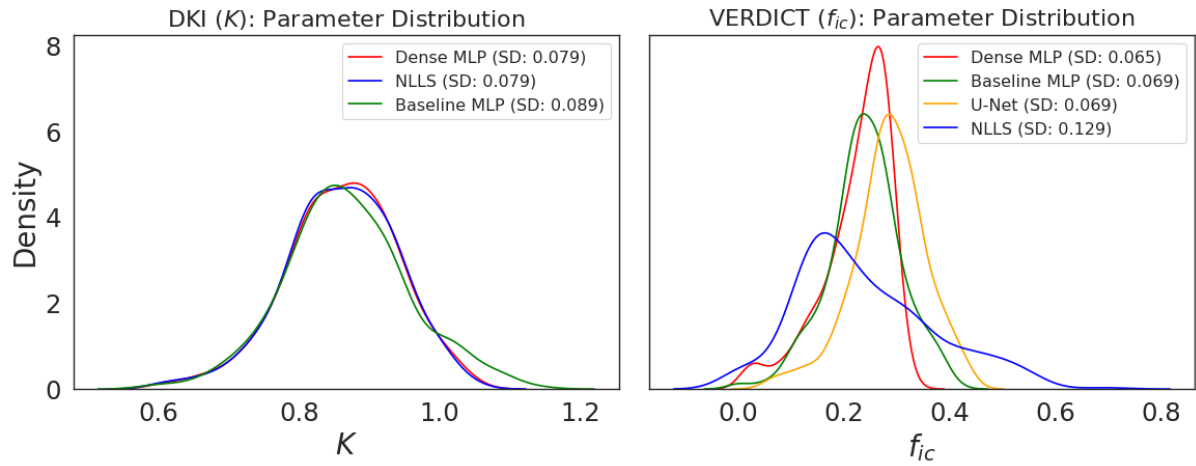


Figure S10: SP1 (300 mT/m): Density plots of K and f_{ic} parameters across diffusion MRI models and fitting methods for all three sub-protocols, with the parameter values aggregated across patients. DKI methods produced highly similar distributions, whereas VERDICT distributions varied across fitting methods. VERDICT Dense MLP showed the lowest pooled standard deviation (SD), whereas VERDICT NLLS exhibited the highest pooled SD.